Acta Materialia 228 (2022) 117751

Contents lists available at ScienceDirect

Acta Materialia

journal homepage: www.elsevier.com/locate/actamat

Data-driven shape memory alloy discovery using Artificial Intelligence Materials Selection (AIMS) framework

W. Trehern, R. Ortiz-Ayala, K.C. Atli, R. Arroyave, I. Karaman*

Department of Materials Science and Engineering, Texas A&M University, College Station, TX, USA

ARTICLE INFO

Article history:
Received 20 February 2021
Revised 9 February 2022
Accepted 10 February 2022
Available online 12 February 2022

Keywords:
Shape memory alloys
Solid-state actuation
Materials informatics
Machine learning
Multi-objective optimization

ABSTRACT

One of the obstacles to the deployment of shape memory alloys (SMAs) in solid-state actuation is the low efficiency and functional instability due to the transformation thermal hysteresis and large temperature ranges during martensitic phase transformation. Numerous studies have been conducted in an effort to minimize the thermal hysteresis and transformation temperature range of SMAs through ternary and quaternary alloying of known binary alloy systems, such as NiTi, and considerable success has been achieved. However, and crucially, the alloys discovered so far have failed to maintain a narrow hysteresis under applied stress. In the present study, an AI-enabled materials discovery framework was successfully used to identify both SMA chemistries and the associated thermo-mechanical processing steps that result in narrow transformation hysteresis and transformation range under an applied stress. The major elements of the proposed workflow are described in detail and its materials-agnostic character makes it widely applicable to other alloy discovery challenges. Using this framework, and without relying on subsequent experimental exploratory analysis, an SMA composition, i.e. $Ni_{32}Ti_{47}Cu_{21}$ (at. %), was predicted and confirmed to have the narrowest thermal hysteresis and transformation range under stress achieved thus far for a NiTi-based SMA. Furthermore, the alloy was shown to exhibit excellent cyclic stability and actuation strain. The methodology and the dataset introduced here can be extended to design novel SMAs with other target functions.

© 2022 Acta Materialia Inc. Published by Elsevier Ltd. All rights reserved.

1. Introduction

Shape memory alloys (SMAs) are excellent candidates for solid-state actuation [1–6] and thermal energy harvesting applications [7–9] due to their capability to undergo reversible, solid-to-solid martensitic phase transformations, with tailorable shape change and energy conversion capabilities. However, irreversible microstructural mechanisms associated with the temperature-induced martensitic transformation introduce inefficiencies that limit their use [10]. Motivated by the potential of low thermal hysteresis SMAs to enable efficient solid-state actuation, a few studies have attempted to tailor the thermal hysteresis by alloying the most well-known NiTi SMAs with elements such as Cu, Pd, Pt, Au, Co, V, Cr, Hf, and Zr [3,11,12]. Furthermore, several studies have shown that thermo-mechanical processing, such as aging heat treatment or cold work followed by low temperature annealing also has an effect on the thermal hysteresis [13,14], but the combined (and potentially synergetic) effects of composition and processing conditions remain unclear.

Thermal hysteresis in SMAs results from irreversible processes during martensitic transformation, including frictional resistance to interfacial motion and dissipation of stored elastic strain energy. Thermal hysteresis leads to different temperatures for forward and reverse transformations, namely martensite start (M_s) and finish (M_f) and austenite start (A_s) and finish (A_f) temperatures. Thermal hysteresis in SMAs is often reported as the difference between the A_f and M_s temperatures measured from differential scanning calorimetry (DSC) thermograms. There have been numerous studies to develop SMA compositions with near-zero thermal hysteresis [4,12], and alloys have been developed with a thermal hysteresis as small as 0.4 °C during stress-free cycling [4,5,15]. However, these alloys have failed to show the same performance under stress, i.e., during actuation [16] or during mechanical load cycling, which are the two main conditions that these materials are desired to operate at.

In addition to minimizing the thermal hysteresis in order to increase the energy conversion efficiency in SMAs, maximizing the reversible shape change (i.e. actuation strain) during martensitic

* Corresponding author.
E-mail address: ikaraman@tamu.edu (I. Karaman).

https://doi.org/10.1016/j.actamat.2022.117751
1359-6454/© 2022 Acta Materialia Inc. Published by Elsevier Ltd. All rights reserved.

transformation is critical to enhance the work output of SMAs as solid-state actuators. To achieve this, complete transformation of the SMA is necessary. Minimizing the transformation range (A_f-M_f), in addition to minimizing thermal hysteresis, allows a higher actuation frequency, as well as less energy input to the system, therefore, a higher energy conversion efficiency for the same useful output. Currently, no literature is available that explores the effect of composition or processing on the transformation range.

To inform the development of SMAs with desired properties, different theoretical and empirical approaches have been proposed to predict the transformation characteristics of SMAs as a function of composition [12,17]. The valence electron concentration ratio has been proposed to be an indicator of composition dependence of M_s temperature [18], but thermal hysteresis does not exhibit such dependence. Both M_s temperature and thermal hysteresis display positive correlation with the latent heat of transformation [11]. A lower M_s indicates higher phase stability of austenite compared to martensite and thus a smaller latent heat between the two phases in a given alloy system [19]. The best-known estimator for the thermal hysteresis associated with the martensitic transformation is the crystallographic compatibility between martensite and austenite phases [12]. Based on the geometric nonlinear theory of martensite, crystallographic compatibility can be described by the middle eigenvalue (λ_2) of the transformation stretch tensor between austenite and martensite lattices. The closer λ_2 is to 1, the lower the chance that defects will form in the vicinity of austenite-martensite interfaces during transformation (indicating good compatibility), and thus the smaller the hysteresis will be [4,12,20–23]. However, this estimator does not account for processing conditions [13,14], microstructural size effects [24,25], or the effect of applied stress on the transformation characteristics and lattice structure [26,27].

In order to take multiple material parameters and external boundary conditions into account, including composition, processing conditions, microstructural size effect, and applied stress, when predicting the thermal hysteresis, materials informatics approaches can be utilized [28]. Materials informatics allows analysis of high-dimensional materials data through machine learning [29,30]. Previously, stress-free transformation temperatures and hysteresis of NiTi-based SMAs have successfully been predicted using materials informatics [31–35]. In CuAl-based SMAs, machine learning was used to identify an alloy with a high transformation entropy change [36]. However, all these efforts focused only on achieving the target properties using only chemical changes and did not consider the role of processing conditions and applied stress on the transformation characteristics. This is an important limitation as processing plays a fundamental role in determining the performance of SMAs.

In the present work, machine learning was used to design an SMA for optimum solid-state actuation and thermal energy harvesting efficiency. Initially, a high-quality dataset was developed to include material composition, processing history and test parameters in order to properly account for all necessary details of every data entry. Utilizing this dataset, the goal was to use machine learning and optimization techniques to (1) minimize the transformation range (A_f-M_f) and (2) maximize the actuation strain under an applied stress (>1.5% strain at an applied stress of 50 MPa or more). In addition to these objectives, the candidate alloy was constrained to operate between $M_f > 20$ °C (cold reservoir is room temperature) and $A_f < 50$ °C. There were no constraints imposed for the composition or processing parameters, allowing for a massive alloy design space with complex processing procedures to be explored.

2. Computational and experimental methods

2.1. Materials informatics framework – Artificial Intelligence Materials Selection (AIMS)

The present study searched for an SMA with a minimum transformation range and an actuation strain of at least 1.5% under an applied stress of 50 MPa or more, using a materials informatics strategy that employed the Artificial Intelligence Material Selection (AIMS) framework introduced here. The AIMS framework uses various machine learning approaches to guide the exploration and discovery of materials (Fig. 1). The process entails extracting and cleaning large amounts of data about the material system of interest from the literature and from high-throughput experiments, using machine learning to discover qualitative and quantitative information about the material system, and making predictions for unknown material compositions and processing parameters. Selected materials are then synthesized, and predictions are compared with experimental data, and the process repeats. Each step is described in more detail below.

Starting from step M1 (denoted by an asterisk* in Fig. 1), literature data extraction serves as the foundation for the framework. This step can be accomplished more efficiently by using a literature mining software [37], tabulation of tables, and plot digitizers [38]. These literature data can also guide any experimental data generation in the laboratory, step M2. These experiments should be conducted using high-throughput batch design techniques and lab automation [39] in order to optimize the workflow. A dataset is then compiled from the literature and high throughput experimental data, and augmented with descriptors based on composition (valence electron number, atomic radii, etc.) (step M3) [40,41].

Data cleaning and initial setup is done by correcting errors, removing duplicate data, and identifying features and responses in the dataset to be used in the analysis. In the case of missing values within the dataset, default values should be defined and used to replace these missing values where possible. Default values should be inserted primarily in the processing features if a sample did not undergo a specific processing procedure. For example, a sample that did not undergo heat treatment might be considered as if it was heat treated at room temperature for 0 h. Categorical features such as the quenching medium after heat treatment need to be encoded to numerical values (water quenching may be given the value of 1, oil quenching given a value of 2, etc.) for analysis (step A1). Before performing any machine learning model training, it is advised that the data are explored and evaluated using feature correlation and dimensionality reduction techniques (step A2) [42,43]. This is an important step to reduce the number of features in the feature set and visualize the spread of the data [44]. In cases where there is an imbalance of classes, the data should be resampled and then split for model training (step A3) [45].

When the data have been prepared for machine learning, tree-based algorithms are used first, allowing for quick model creation and evaluation (step I1) [46]. This step can provide valuable insights into the data, such as feature importance, and identify any outliers that may need to be checked. The iterative model training process includes both feature engineering and hyperparameter tuning, which should be performed for each model that is trained (step I2) [47]. At this point, other algorithms may be employed, such as neural networks or Gaussian process regressors, to predict new material properties. These predicted data should then be visualized with the real data inlayed into the prediction visualization for comparison (step I3).

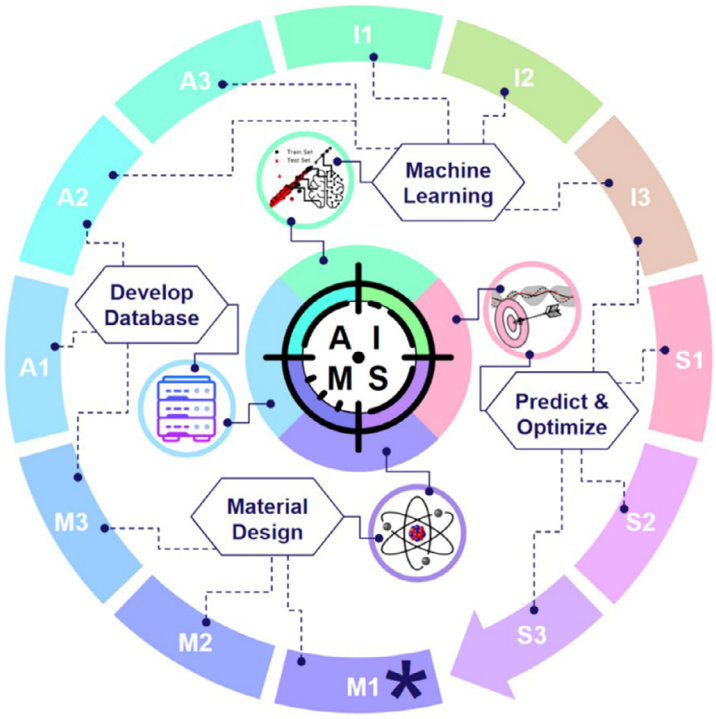

AIMS: Artificial Intelligence Materials Selection	
M1	*Literature Data Extraction*
M2	*High Throughput Synthesis*
M3	*Database Creation*
A1	*Data Preparation*
A2	*Explore and Visualize*
A3	*Data Sampling and Splitting*
I1	*Initial Model Creation*
I2	*Model Refining and Tuning*
I3	*Predict and Visualize*
S1	*Optimization*
S2	*Materials Selection*
S3	*Design of Experiments*

Fig. 1. The Artificial Intelligence Materials Selection (AIMS) framework that captures the iterative workflow necessary for data-driven discovery in materials science.

When there are multiple target properties, a multi-objective optimization approach may prove useful in conjunction with Bayesian Optimization or Natural Selection Genetic Algorithms (step S1) [48–52]. It may also be useful to develop a Pareto front to better visualize and understand tradeoffs made in the material predictions. Based on the optimization results, the selected material should be evaluated by a metric for novelty and feasibility (often by consulting phase diagrams) (step S2). Once a material has been identified, the best candidate alloy can be synthesized, or a design space can be created bounded by constraints in the material composition and processing procedures space (step S3). Within these bounds, Design of Experiments (DOE) can be performed to explore the material characteristics within the regions of interest [53]. In this way, the AIMS framework can be employed to exploit large amounts of materials data over a wide design space to guide materials designers to a more targeted space for further exploration and materials discovery.

2.2. Deploying AIMS framework for SMAs

Following the AIMS framework, the results from raw experimental data for NiTi-based SMAs with various alloying elements (~6000 data entries from 16 years of experiments generated in the authors' laboratory) were tabulated into a spreadsheet (steps M1-M2 in Fig. 1). For all data entries, the composition, processing conditions, test parameters, and material response were recorded. Any variation in composition, processing, and test parameters (such as varying stress levels) are recorded as separate data entries. These results included data from all SMA compositions and processing conditions tested, regardless of whether they exhibit phase transformation or not, which is important for quantifying uncertainty for data entries. Literature data (~250 data entries) for various compositions were also added to supplement the dataset [3,4,10–26,31–33,36,54–88]. The dataset was then cleaned, and new descriptors based on the chemistry were added, such as the atomic number and number of valence electrons (step M3, A1). For this work, descriptors were found from pure element properties available in the periodic table. Supplementary Table S2 lists all descriptors and information regarding the identification information and the status after performing feature correlation. In all, for each distinct material data point, the dataset included 88 features related to the materials composition, processing, and test parameters, along with 26 material responses related to the functional properties and microstructure characteristics. In this analysis, the microstructure data is used to assess discrepancies within the dataset, but is not used as a feature nor response in the machine learning models. A complete list of features, descriptors, and materials responses included in the dataset is summarized in Fig. 2 and can also be found in the supplementary information (Supplementary Tables S1 and S2).

Upon completion of the dataset, Pearson correlation was used to identify and remove extraneous descriptors that were highly linearly correlated (step A2). Of the 59 descriptors in Supplementary Table S2, 31 of the descriptors were highly correlated with other descriptors with absolute correlation values of greater than 0.85 (Fig. S1 in supplementary). These features were removed from the dataset, resulting in the final Pearson correlation matrix at right in Fig. S1. Next, Principal Component Analysis (PCA) [89] was used to transform the high dimensional space to principal components. A scree plot was created, plotting the principal components against the Explained Variance Ratio (ratio of variance that is attributed by each of the principal components) (Fig. S2A in supplementary materials). The two components that explain the most variance, principal components 1 and 2, were plotted against each other in a biplot shown at right in Fig. S2B in supplementary materials. The data points are colored by the Martensite Start (M_S) temperature.

Upon inspection of the reduced dimensional space, large differences for material responses in neighboring data entries were identified and evaluated on a case-by-case basis to determine if the flagged data entries were outliers and/or conflict with the known physical principles. The points in the red circle (Fig. S2B.) are for NiTiHf shape memory alloys and were expected to have

Table 1
Transformation temperatures of $Ni_{32}Ti_{47}Cu_{21}$ and $Ni_{80-X}Ti_XCu_{20}$ (X = 40, 42, 44, 46, 48, 50) as measured from the 2nd cycle differential scanning calorimetry (DSC) data.

Ni (at%)	Ti (at%)	Cu (at%)	M_f(°C)	M_s(°C)	A_s(°C)	A_f(°C)	Transformation Range (A_f-M_f) (°C)
40.0	40.0	20.0	-62.3	-22.2	-49.4	-8.1	54.2
38.0	42.0	20.0	-25.6	-12.1	-13.5	0.7	26.3
36.0	44.0	20.0	-4.6	4.7	4.5	16.1	20.7
34.0	46.0	20.0	6.9	17.5	16.1	28.4	21.5
32.0	48.0	20.0	17.2	23.3	26.3	34.4	17.2
30.0	50.0	20.0	70.3	78.3	79.1	85.2	14.9
32.0	47.0	21.0	31.7	37.3	36.7	41.2	9.5

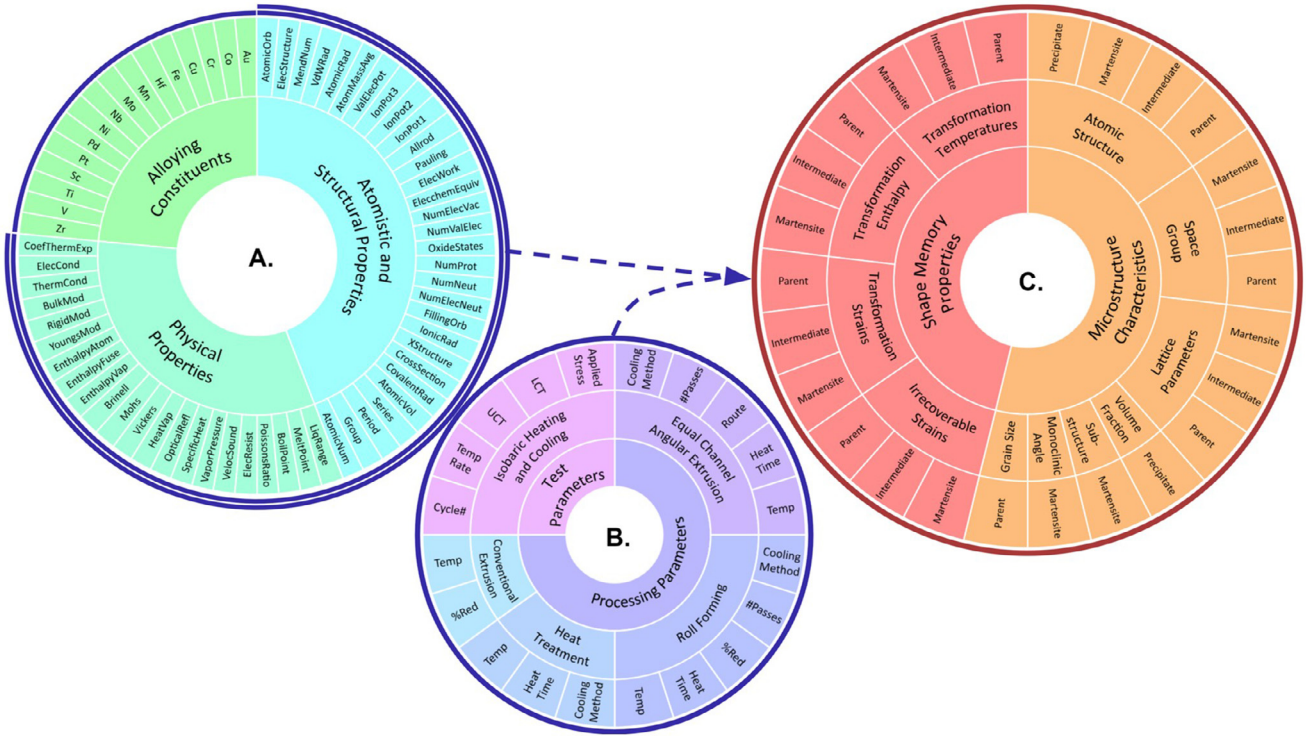

Fig. 2. Sunburst charts illustrating the breakdown of the shape memory alloy dataset developed. All 88 features, circles (A) and (B), visualized by composition, materials descriptors (double dark blue bar), processing, and test parameters. All 26 material responses, circle (C), include functional properties and microstructure characteristics (For interpretation of the references to color in this figure legend, the reader is referred to the web version of this article).

high M_S temperatures. However, these data points showed significantly lower transformation temperatures than other similar NiTiHf compositions. Upon inspection of the group of data, the NiTiHf samples were from the same experimental batch, indicating processing or testing complications associated with the results. It was determined that the set of samples were not subjected to a homogenization heat treatment after casting, dramatically changing the observed transformation temperatures in comparison to similar compositions in the dataset. These data points were removed from the data set.

Next, the cleaned data is prepared for training the initial machine learning models. In the case of an unbalanced number of sample compositions or processing procedures (e.g., 300 data points for solution heat treated samples, but only 40 data points for cold-rolled samples), the lesser number of samples must be oversampled, the greater number of samples must be undersampled, or a mixture of the two (step A3). In this case, the Synthetic Minority Over-*sampling*Technique (SMOTE) was employed to over-sample the data by creating synthetic material responses with Gaussian noise [90] for various composition and processing parameters. The dataset was then split 80/20 (80% for training and 20% for testing), and multiple regression models were trained on the training data to predict the desired material responses (M_f, A_f, actuation strain, and transformation range).

Initial model creation and training with XGBoost [91], a popular decision-tree regression technique, was performed to evaluate model fit and quickly identify important features (step I1) (Fig. 3). The XGBoost regressor identified the average enthalpy of fusion and average Mendeleev number as the two most important features for predicting the transformation range (Fig. 3D). From these results, the top 20 important features (shown in Tables S1 and S2 in supplementary materials) were then used to train three different machine learning regressors. Random Forest, Extreme Gradient Boosting, and Deep Neural Network regressors were fit to the data, and hyperparameters were tuned using Hyperopt [92] for each model and for each desired material property. For the neural network, a rectified linear unit (ReLU) activation function was used at each layer [93]. L2 regularization and dropout [94] was used with an optimum dropout rate of 0.4 to prevent model overfitting. Early stopping was also used to improve model robustness and the loss was analyzed with the binary cross-entropy (CE) method [95], comparing the real and predicted properties and updating the weights and biases through back propagation and gradient descent in order to minimize the loss function. The results of 80% training

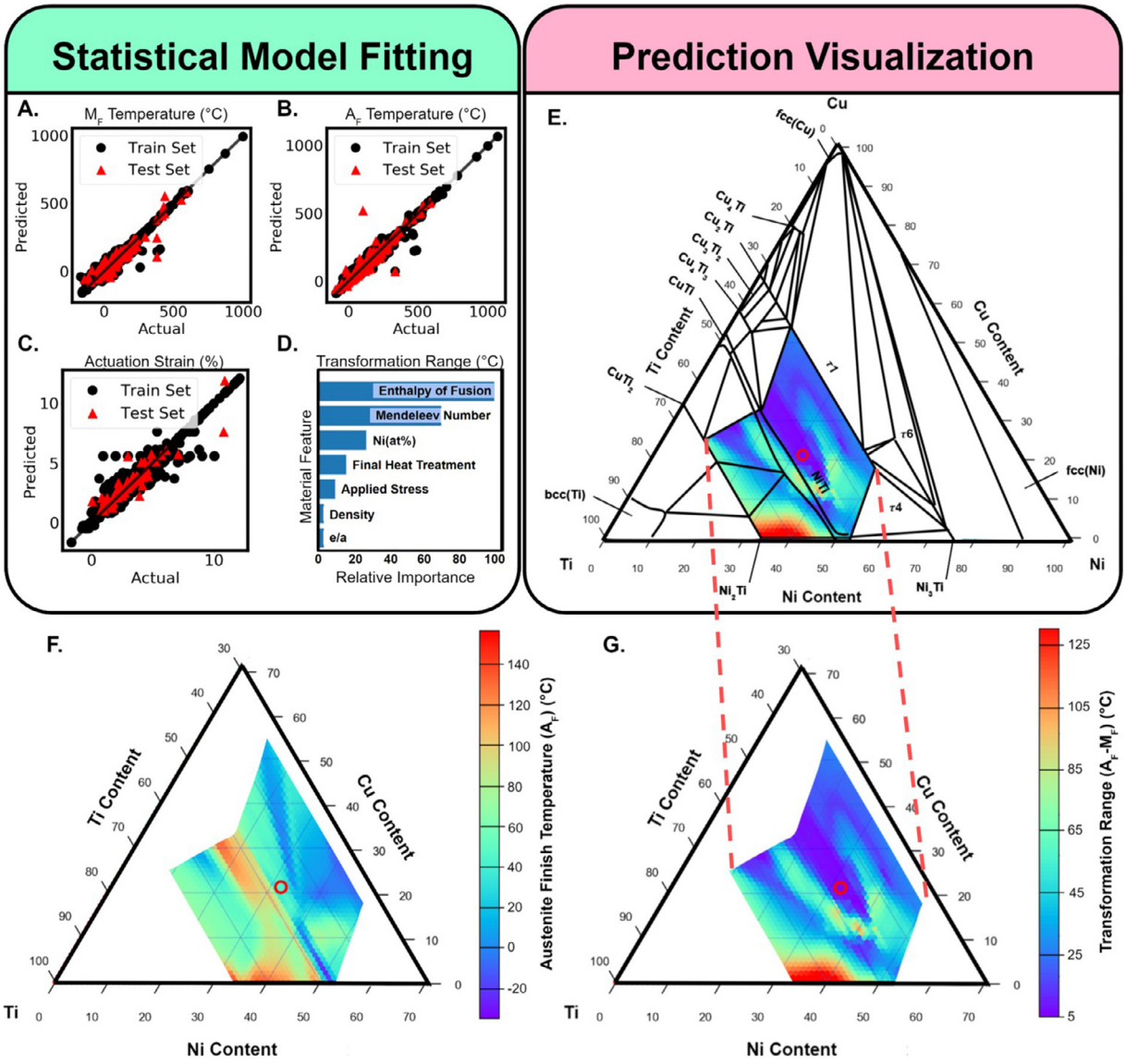

Fig. 3. The performance of the trained Extreme Gradient Boosting (XGB) regression model in predicting the martensite finish (M_f) (A) and austenite finish (A_f) (B) temperatures, and actuation strain levels (C) of NiTi-based shape memory alloys. The important material features in the dataset for predicting the transformation range (A_f – M_f), determined using parameter sensitivity analysis with Extreme Gradient Boosting regression, (D), and the optimal prediction region from the deep neural network (DNN) regressor, overlayed with the NiTiCu ternary phase diagram [100] (E). Scaled ternary diagrams for the DNN regressor predictions of A_f (F) and transformation range (G) are also shown.

data and 20% testing data for each of the three model types can be seen in Fig. 5A and performance metrics (measured by Mean Absolute Error and Root Mean Squared Error) are summarized as bar charts in Fig. 5B (step I2). Based on the model performances, the deep neural network, developed using Keras [96] and Tensorflow [97], was selected for further analysis.

Iterative predictions were made for M_f, A_f, actuation strain, and transformation Range (A_f - M_f) as a function of composition, processing, and, importantly, thermo-mechanical testing parameters using the deep neural network (step I3). The test parameters included applied stress levels of 0 MPa to 300 MPa in order to evaluate the performance of the predicted compositions and estimate the change in transformation range under applied stress. Many of the predicted compositions with theoretically small transformation range were found out to lie outside the original dataset composition space, allowing the discovery of new alloys. The predictions were then constrained by the design requirements ($M_f > 20$ °C, $A_f < 50$ °C), and any predictions outside these bounds were eliminated. For alloy selection, a weighted-sum (75% for transformation range, 25% for actuation strain) multi-objective Bayesian optimization was used (S1) to determine which predictions would have the highest Expected Improvement (EI) for the transformation range (minimization) and actuation strain (maximization).

2.3. AIMS predictions for SMAs

In general, the results predicted that alloying NiTi with Cu, Pd, and Au would exhibit the best results in terms of narrow thermal transformation ranges. However, NiTiPd and NiTiAu alloys were not pursued due to the high cost, elevated transformation temperatures, and increase in transformation range under an applied stress [61,64,98]. NiTiCu was predicted to have a small transformation range (Fig. 3E and G) and good actuation strains within the design constraints. The best predicted performance within the NiTiCu system was for $Ni_{32}Ti_{47}Cu_{21}$ (at. %) with a predicted homogenizing heat treatment of 925 °C for 48 h and hot rolling reduction to

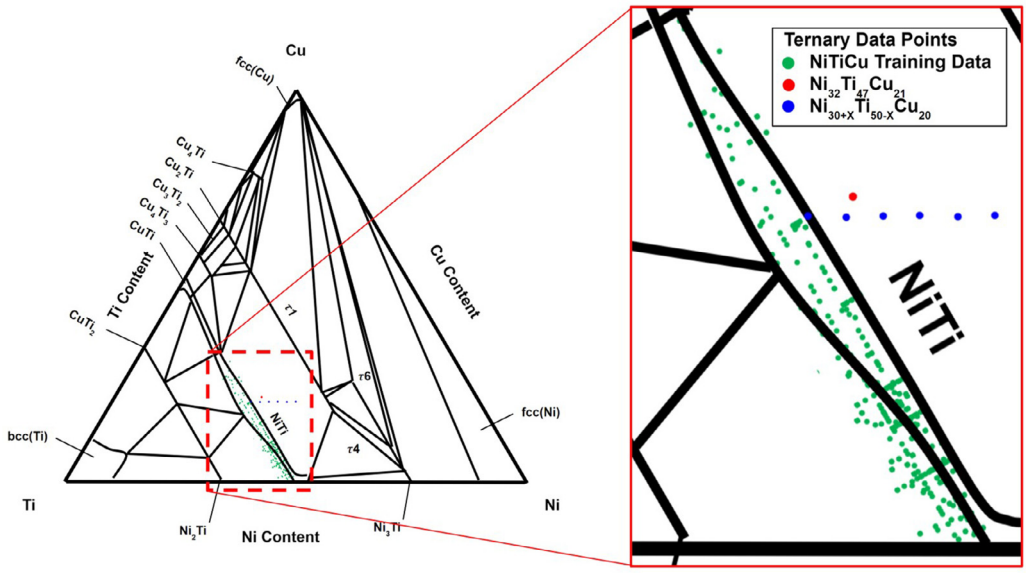

Fig. 4. NiTiCu ternary phase diagram visualization [100] with training data used in the machine learning model (green), the predicted optimal composition (red), and other NiTiCu validation points (blue).

20% at 850 °C (predicted transformation range of 7 +/- 4 °C and predicted actuation strain of 2.0 +/- 0.5% under 50 MPa stress). This result was surprising and completely unexpected, as Cu typically substitutes Ni, and Ti is usually held at 50 at.% for conventional NiTiCu SMAs [73,74]. The compositions of NiTiCu that were present in the training data (Fig. 4) lie primarily in the single-phase region of the phase diagram. Predictive capabilities outside traditional alloy composition design space further justify the usefulness of machine learning in materials design. NiTiCu predictions for martensite finish, austenite finish, transformation range, and actuation strains for varying heat treatment temperatures (425 °C to 925 °C) and varying stresses (50 MPa to 300 MPa) can be found in the supplementary materials. In addition, NiTiCu-X (X: Pd, Au, and Hf) predictions (incrementing by X content) are also visualized in the supplementary text (Supplementary Tables S6–S8).

2.4. Alloy fabrication and thermomechanical characterization

The predicted optimal material $Ni_{32}Ti_{47}Cu_{21}$ was then fabricated and experimentally characterized, and the experimental results and predictions were compared (S3). In addition to $Ni_{32}Ti_{47}Cu_{21}$, several other Ti-lean NiTiCu samples were synthesized and compared. The compositions were arc melted from high purity raw materials (>99.99%), in an argon atmosphere. The alloy buttons (60 g) were flipped and remelted 5 times, sealed in a quartz tube under argon, and homogenized at 925 °C for 48 h, and hot rolled at 850 °C to 20% reduction in thickness, as predicted by the machine learning model. The material was then cut using wire electrical discharge machining (wire-EDM) to extract a 3 mm-diameter x 1 mm-thick differential scanning calorimeter (DSC) specimen and dog-bone-shaped tensile testing specimens with gage dimensions of 8 mm x 3 mm x 1.0 mm. The specimens were polished to 1 μm surface finish prior to testing to remove the possible effects of an EDM recast layer. A TA Instruments Q2000 Differential Scanning Calorimetry (DSC) was used to determine the stress-free phase transformation temperatures of the arc melted button. The material was thermally cycled 2 times at a heating-cooling rate of 10 °C min^{-1}. Stress-free transformation temperatures were determined from the DSC peaks using the slope line extension method as described in ASTM F2004-17. The latent heat of transformation was also calculated from the area under the transformation peaks.

Isobaric heating and cooling experiments were performed on the $Ni_{32}Ti_{47}Cu_{21}$ SMA in an effort to characterize its transformation behavior, including the evolution of transformation temperatures, actuation strain (measured as the strain recovered during reverse transformation), irrecoverable strain (measured as the open loop strain at the upper cycle temperature) and thermal hysteresis (measured as the width of the strain vs. temperature loop corresponding to one half the transformation strain) as a function of stress. Tests were performed on a servo-hydraulic MTS test frame. Strain was measured using a high-temperature extensometer directly attached to the gage section of the samples. Samples were heated through conduction from the grips with heating bands. Cooling of the samples was achieved by conduction by flowing liquid nitrogen through copper tubes wrapped around the grips. The rate of heating and cooling during mechanical testing was 10 ± 2 °C min^{-1}. The temperature was measured using a K-type thermocouple, directly attached to the gage section of the samples. Test was initiated by heating the specimen to 125 °C and then loading to 2 MPa (a small stress level enough to ensure whether the specimen transforms within the selected temperature range without causing transformation induced plasticity). The specimen then undergoes a single thermal cycle (cooling to 0 °C and then heating back to 125 °C) while maintaining the applied stress. Upon completion of the thermal cycle, the load is increased by 50 MPa and another thermal cycle is performed under constant stress. This procedure is repeated until specimen fails.

For constant-stress thermal cycling experiments, a custom-built test frame was used to cycle the sample 800 times. 50 MPa was applied to the $Ni_{32}Ti_{47}Cu_{21}$ SMA through a dead load hanging from the bottom grip. Heating of the sample was performed through conduction from inductively heated grips. Cooling was performed through convection using a muffin fan. Heating and cooling rates during thermal cycling were maintained at approximately 65 °C min^{-1} and 35 °C min^{-1}, respectively. Displacement was measured using a linear variable differential transformer (LVDT) and recorded displacements were converted into strain taking the 8 mm initial gauge length of sample as reference.

The microstructure of the samples was observed using FEI Quanta 600 FE-SEM with a voltage of 15 kV. Oxford energy dis-

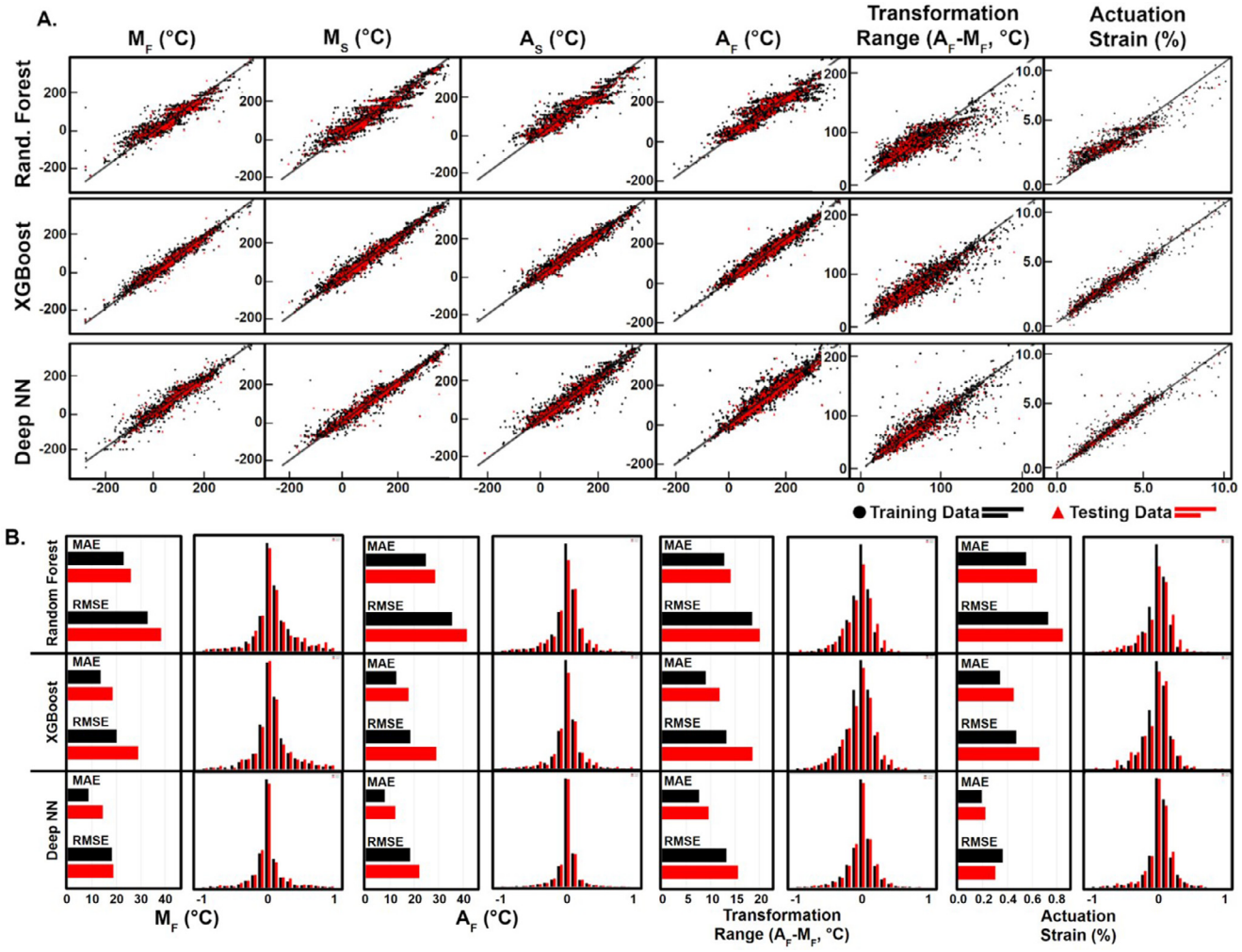

Fig. 5. Visualization of machine learning regressor model fitting to the shape memory alloy data set (A) and respective error metrics and histogram of residual errors (B). 80% of the data was used to train the model and 20% of the data was used to test the model performance. MAE: Mean Absolute Error, RMSE: Root Mean Squared Error.

persive X-ray spectroscopy (EDS) system equipped with X-ray mapping and digital imaging was used to determine the composition of the matrix and the second phase present in the homogenized and hot rolled samples. The second phase area fraction was quantified using ImageJ software for the backscatter electron images.

3. Results and discussion

3.1. Thermomechanical characterization results

The predicted and experimental DSC results for $Ni_{32}Ti_{47}Cu_{21}$ (Fig. 6A) showed a transformation range of ~9.5 °C (A_f = 41.2 °C, M_f = 31.7 °C) with the latent heat of transformation for martensite (M) to austenite (A) transformation of $dH_{M\text{-}A}$= 14.89 J/g and for austenite to martensite transformation of $dH_{A\text{-}M}$=14.71 J/g. This transformation range differs from the predicted by 2.5 °C, which is within the prediction standard deviation (7 +/- 4 °C). This is a remarkable agreement considering the large differences in transformation ranges observed in SMAs. The other Ti-lean compositions were tested in DSC, and the results are tabulated (Table 1) and compared with the respective predictions in Fig. 7. It is clear that $Ni_{32}Ti_{47}Cu_{21}$ exhibits a smaller transformation range than the other Ti-lean NiTiCu samples, with 5.4 °C decrease from the smallest transformation range Ti-lean sample.

The predictive capabilities of the model remain accurate even in the presence of an applied stress. We note that known estimators, such as the middle eigenvalue (λ_2) of the transformation stretch tensor between austenite and martensite lattices, are unable to predict the thermal hysteresis or transformation range under stress. This is especially true for more ductile SMAs, such as Cu-based ones, which exhibit thermal cyclic instability under stress as defects form more readily, increasing frictional resistance to interfacial motion. In addition, the differences in the elastic constants of austenite and martensite phases influence the thermal hysteresis and transformation range under stress, with different elastic deformation levels occurring in the two phases during thermal cycling with an applied stress, leading to changes in the compatibility between the transforming phases. Furthermore, plastic accommodation and relaxation of coherency strains as an interface bypasses dislocations and precipitates causes dissipation of elastic strain energy, leaving less elastic strain energy to assist the reverse transformation, increasing the thermal hysteresis of an SMA [27].

$Ni_{32}Ti_{47}Cu_{21}$ was then thermally cycled under different tensile stresses to determine the stress vs. temperature phase diagram (Fig. 6C). It is observed that below 150 MPa, the SMA undergoes a fully reversible transformation exhibiting no irrecoverable strain. The maximum value of actuation strain was recorded as ~2% at 200 MPa at the expense of a 0.2% irrecoverable strain. Transformation range under 2 MPa is 5.3 °C, which is even smaller than the one measured from DSC results, and increases with increasing applied stress, reaching 7.8 °C at 50 MPa and finally exceeds 20 °C at 200 MPa.

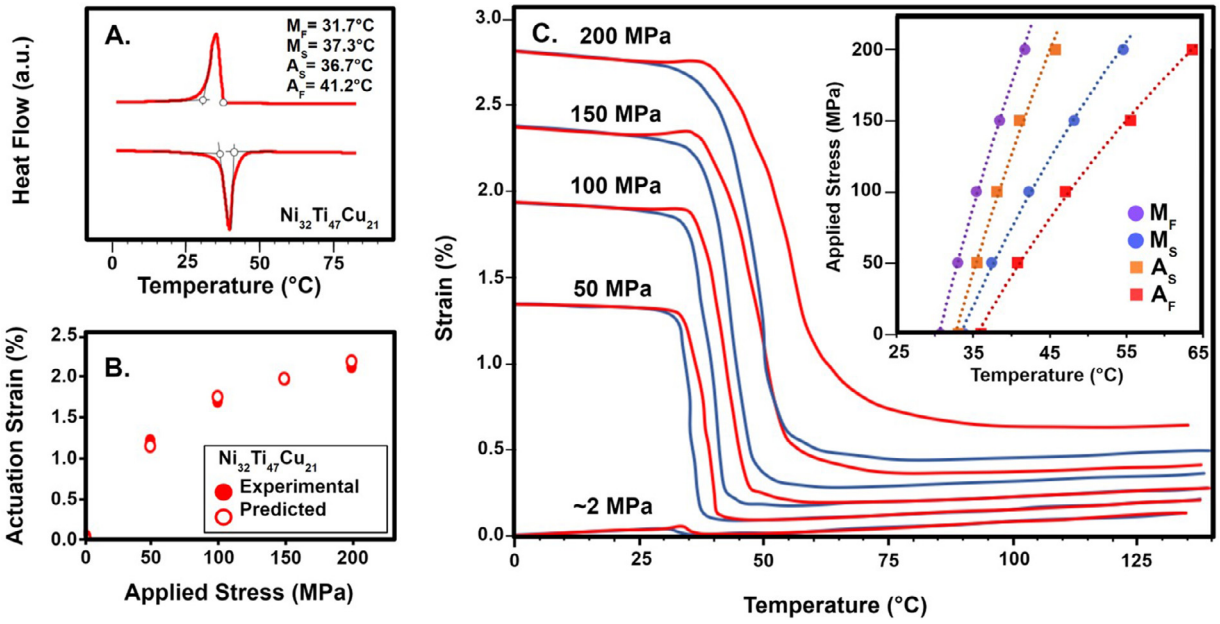

Fig. 6. (A) Differential Scanning Calorimetry (DSC) thermogram for the designed and fabricated $Ni_{32}Ti_{47}Cu_{21}$ shape memory alloy. (B) Predicted and experimental actuation strains under various stress levels. (C) Isobaric heating cooling test results under various stress levels and corresponding stress vs. temperature phase diagram constructed using this data. The Clausius-Clapeyron (CC) slope for M_f, M_s, A_s, and A_f is calculated as 18.1 MPa/°C, 15.9 MPa/°C, 9.5 MPa/°C, and 7.1 MPa/°C, respectively.

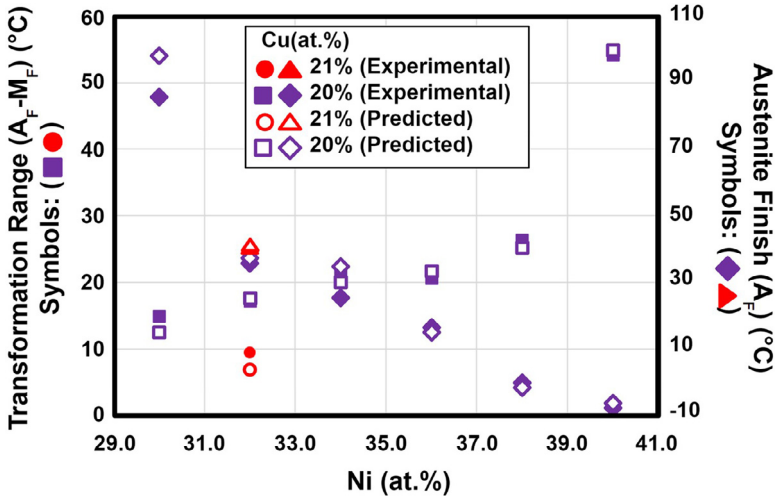

Fig. 7. Comparison of the predicted and experimental martensitic transformation ranges and austenite finish temperatures confirmed by DSC for the designed and fabricated NiTiCu shape memory alloy compositions in this study. All samples have the same processing history.

The actuation strains as predicted by the deep neural network are remarkably close to the experimental actuation strains (Fig. 6B). The actuation strains are generally lower than other NiTi-based alloys due to the single stage martensitic transformation from cubic (B2) to orthorhombic (B19) in NiTiCu compositions with Cu content greater than 20 at.% [99], which may have contributed to the models high predictive accuracy considering the small range of actuation strain values. The model captures the change from cubic-monoclinic (<20 at.%) to cubic-orthorhombic (>20 at.%) martensitic transformations well for both transformation range and actuation strains (shown in supplementary materials). This indicates a trade-off between large actuation strains (for Cu<20 at.% showing B2-B19') and small transformation ranges (for Cu>20 at.% showing B2-B19). This insight is not only a testament of machine learning predictive capabilities, even in the absence of microstructural data, but also demonstrates a need for interpretation of predictions through scientific reasoning.

Based on the stress vs. temperature phase diagram, a stress level of 50 MPa was selected for constant-stress thermal cycling experiments since the alloy satisfied the transformation temperature boundary conditions at this stress level (M_f > 20 °C and A_f < 50 °C). Specimens were subjected to 800 thermal cycles under 50 MPa constant stress, revealing 1.7% actuation strain, excellent cyclic stability, 5.2 °C thermal hysteresis under stress, and 16.7 °C transformation range under stress at the end of the 800 cycles (data for strain evolution shown in Fig. 8A, the last 5 cycles are shown in Fig. 8B). Inarguably, SMAs with such cyclic stability and extremely narrow thermal hysteresis under stress would be ideal materials for actuation applications near ambient temperatures and especially for thermal energy harvesting applications, where low temperature gradients are encountered.

The $Ni_{32}Ti_{47}Cu_{21}$ sample is in the two-phase region of the phase diagram [100] and is expected to show $(Cu, Ni)_2Ti$ precipitates. The microstructure was confirmed to have the $(Cu, Ni)_2Ti$

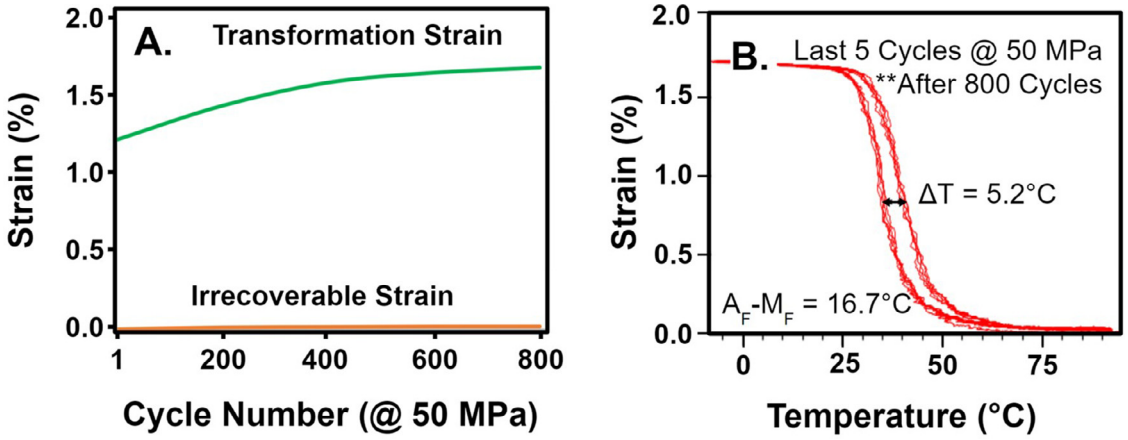

Fig. 8. A. Constant stress heating and cooling results at 50 MPa showing the transformation strain and irrecoverable strain evolution with thermal cycling. B. The last 5 cycles of the constant stress experiment showing transformation strains of 1.7%, no irrecoverable strain, 5.2 °C thermal hysteresis and 16.7 °C transformation range.

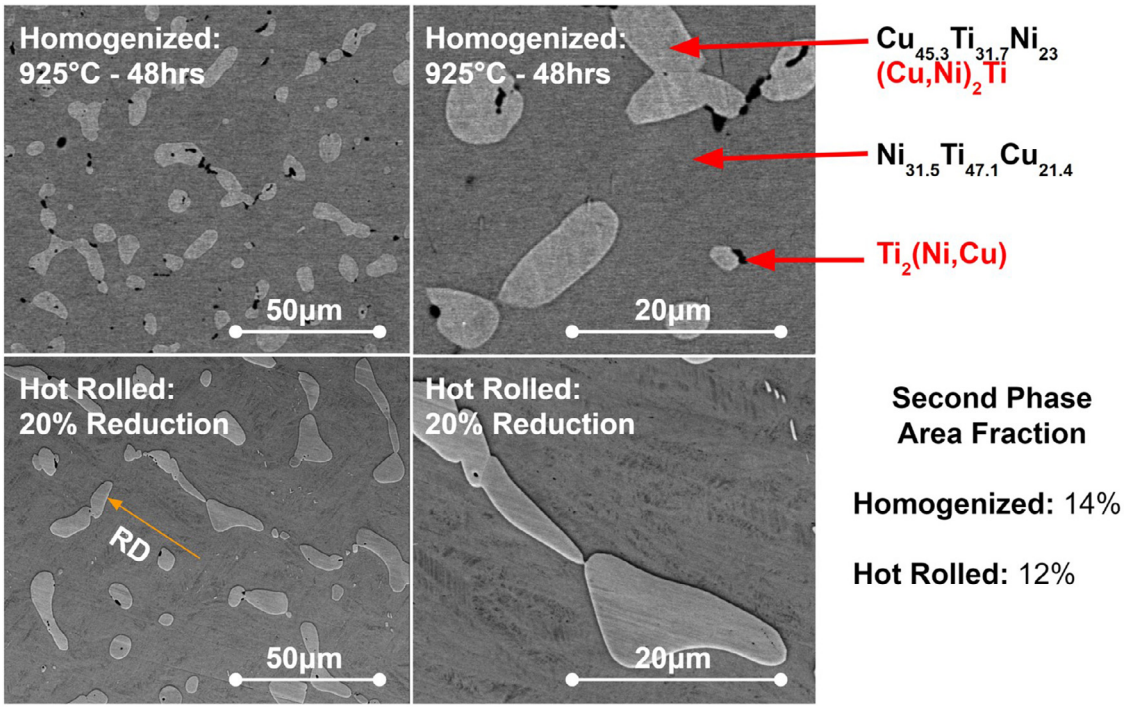

Fig. 9. Backscattered Electron (BSE) images of the homogenized and hot rolled $Ni_{32}Ti_{47}Cu_{21}$ samples. The second phase particles appear slightly elongated in the rolling direction (RD). Compositions of the matrix and second phase were confirmed with energy dispersive X-ray spectroscopy (EDS).

precipitates with an area fraction of 14% after heat treatment as seen in SEM/BSE images with composition confirmation using EDS (Fig. 9). After hot rolling, the precipitates are slightly elongated in the rolling direction (RD), retaining a similar second phase area fraction of 12%. In addition to the inherent lattice compatibility in NiTiCu alloys, it is likely the internal stresses at the interfaces between the transforming matrix and $(Cu,Ni)_2Ti$ precipitates help to enable the B2↔B19 transformation to follow the same low energy path during each thermal cycle [101,102], yielding excellent cyclic stability and small transformation range.

3.2. Comparisons with other NiTi-based alloys

The data for the $Ni_{32}Ti_{47}Cu_{21}$ alloy and various other NiTi based alloy systems from the dataset were plotted against the two most important features for the transformation range as identified by XGBoost (Fig. 10). The features identified as the third and fourth most important ones – Ni content (at. %) and final heat treatment in Fig. 3D – are also indirectly considered by plotting only solution treated alloys in Fig. 10 that are equiatomic, based on the elemental substitutions. The important features exhibit distinct separate regions for the compositions and the transformation ranges, indicating that these features identified with the XGBoost regressor greatly impact the transformation range for different alloy compositions. The Mendeleev number is an ordering number attributed to each chemical element, ordering them by similar properties (using the chemical scale) along a singular axis [103,104]. The importance of average enthalpy of fusion may not have any physical meaning, however, it allows for compositional mapping of different SMA compositions and separation of high and low transformation ranges in a single dimension. These results point to a chemical space that holds promise for future efforts to design SMAs with narrow transformation ranges.

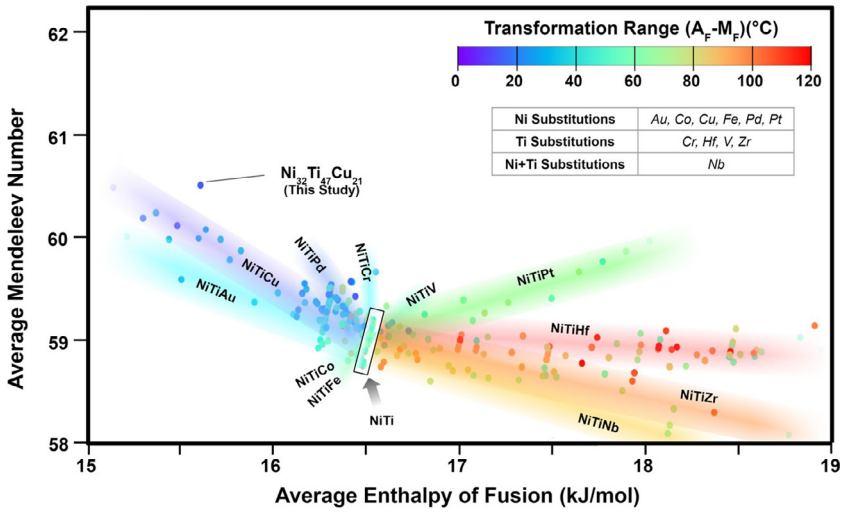

Fig. 10. Transformation range of the solution heat treated, equiatomic (by substitution) data entries for all NiTi-based shape memory alloys in the newly developed dataset on shape memory alloys, visualized as a function of the two most important materials features identified by the parameter sensitivity analysis for the Extreme Gradient Boosting regression model. The two important features, average enthalpy of fusion and average Mendeleev number, were calculated using simple rule-of-mixtures, using each element contribution to the total alloy composition. The features do not represent any chemical or physical meaning, however, they separate the compositions into low (on the left) and high (on the right) transformation ranges. The result for the designed and experimentally validated NiTiCu alloy is also shown.

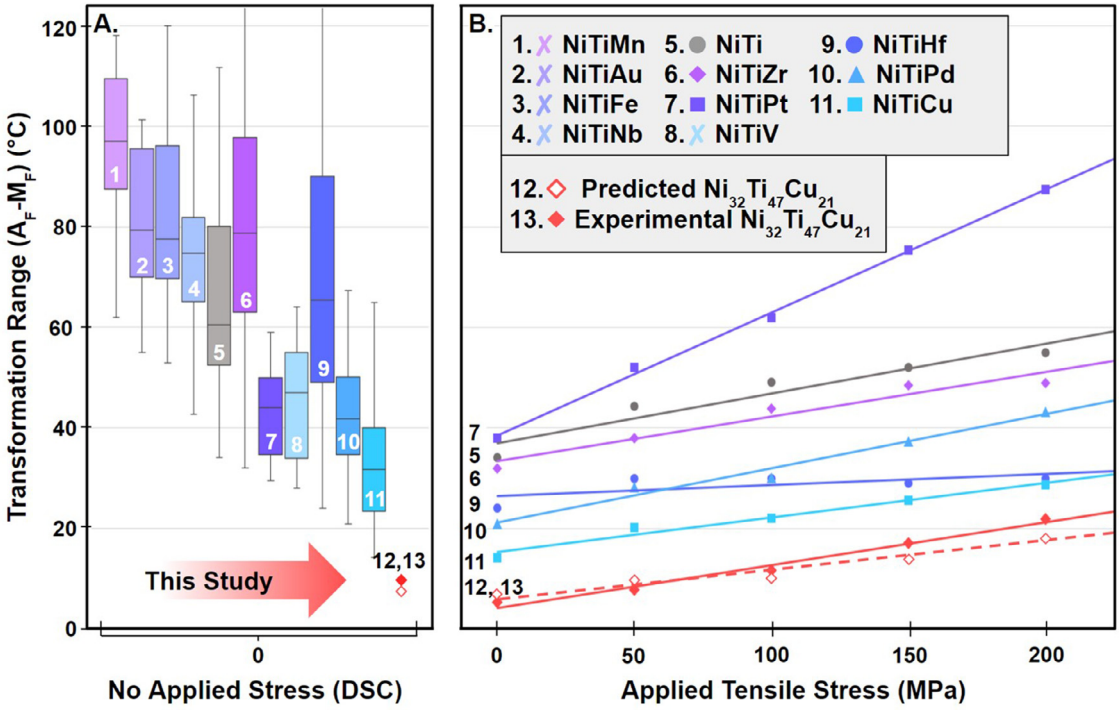

Fig. 11. (A) Box plots for the transformation range of various shape memory alloy compositions from the newly developed shape memory alloy dataset together with the predicted and experimental results of the NiTiCu alloy designed using the Artificial Intelligence Materials Selection (AIMS) framework. (B) The minimum transformation range under applied stress for various alloy compositions. Predicted and experimental results of the NiTiCu alloy of the present study are shown in red.

The measured transformation ranges under zero applied stress (in DSC) for various NiTi-X compositions are visualized as a box-plot in Fig. 11A. Compared to other NiTi-X compositions tested in DSC for bulk specimens, the $Ni_{32}Ti_{47}Cu_{21}$ alloy designed, fabricated and tested in this study (#12 (predicted) and #13 (experimental), in red) exhibited the narrowest transformation range. The well-known, near-zero thermal hysteresis SMA composition, $Ti_{50.2}Ni_{34.4}Cu_{12.3}Pd_{3.1}$, has no visible hysteresis in electrical resistivity measurements, however, in DSC the alloy shows a transformation range of ~27 °C and a thermal hysteresis of ~15 °C [15]. The resistivity of the austenite (B2) and martensite (B19) phases are very similar for the $Ti_{50.2}Ni_{34.4}Cu_{12.3}Pd_{3.1}$ sample, which resulted in a very subtle change during martensitic transformation [15]. However, the reasons for the differences in SMA transformation characteristics between the DSC and resistivity measurements are not very well known. In comparison, we present in this work the $Ni_{32}Ti_{47}Cu_{21}$ alloy with a transformation range of 9.5 °C and thermal hysteresis of 3.9 °C as confirmed by DSC.

The isobaric heating and cooling at various stress levels indicates that the $Ni_{32}Ti_{47}Cu_{21}$ alloy under 50 MPa shows a transformation range of 7.8 °C, a thermal hysteresis of 3.2 °C, and fully recoverable transformation strain of 1.2%. In the case where higher

actuation strain is desirable with slightly elevated transformation temperatures, 100 MPa will yield a transformation range of 11.5 °C, thermal hysteresis of 3.5 °C, and fully recoverable transformation strain of 1.7%. The dislocations at stress levels above 100 MPa lead to significantly larger transformation ranges and irrecoverable strains, for example, at 150 MPa the transformation range increases to 17.1 °C, thermal hysteresis increases to 6.5 °C, and transformation strain is 2.03% with irrecoverable strain of 0.07%. With an applied stress, the $Ni_{32}Ti_{47}Cu_{21}$ alloy retains the small transformation range whereas many other NiTi-based alloy compositions with small transformation range and hysteresis do not. For comparison, a $Ti_{50}Ni_{33.5}Cu_{12.5}Pd_4$ sample at 47.6 MPa has a transformation range of 25 °C, thermal hysteresis of 15 °C, and actuation strain of 1.47% [16].

Available experimental data for the minimum transformation ranges measured under tensile stress during isobaric heating and cooling experiments were plotted for each composition, shown in Fig. 11B. Under an applied stress, the $Ni_{32}Ti_{47}Cu_{21}$ alloy identified in this study showed a 6 °C lower transformation range than the nearest NiTi-X alloy. The predicted transformation range at lower stress levels is slightly more accurate than at higher stress levels (Fig. 11B). This could be due to the model's inability to accommodate for the accumulation of irrecoverable strain and defect formation at each stress level, effectively increasing the transformation range in the material. For visualization of all predictions in this work, refer to the supplementary materials for the predicted ternary diagrams for all targeted properties in NiTiCu for various stress levels and for heat treatments.

4. Summary and conclusions

The Artificial Intelligence Materials Selection (AIMS) framework in this work was successfully deployed for guiding materials informatics and machine learning approaches in SMAs. The material-agnostic framework can also be utilized in other datasets to analyze and predict within various material systems. Information can also be attained through the use of material descriptors and feature engineering, aiding in discovery of new composition-processing-property relationships. The iterative workflow allows for the navigation through high dimensional material spaces and rapid development of materials with targeted properties.

Here, a shape memory alloy (SMA) that maintains a narrow thermal hysteresis and transformation range under stress was identified by employing AIMS and a new SMA dataset developed with more than 6000 discrete experimental data points. This work has outlined all necessary information for the creation of an SMA database for use in machine learning, and this study has also proven the need for interpretation of machine learning predictions through scientific reasoning. This work is also the first to model the transformation range and actuation strains for various stress levels in SMAs. These target material properties are two of the most important properties to optimize when designing an SMA for actuator applications. A region showing promise for designing future SMAs with narrow transformation ranges was also mapped for the Enthalpy of Fusion and the Mendeleev Number, guiding potential studies in the future iterations of AIMS for SMAs.

The fabrication and experimental characterization of the designed alloy demonstrated the lowest transformation range and thermal hysteresis under an applied tensile stress reported thus far for NiTi-based SMAs, as well as excellent cyclic stability, agreeing very well with the predictions of the machine learning model. All generated predictions for NiTiCu (supplementary material) can provide valuable transformation characteristics for the entire NiTiCu system to aid other research in alloy design. These results also indicate that SMA technology can efficiently work at very low temperature gradients and also show promise for low-grade thermal energy harvesting applications.

Data availability

The data supporting the findings in this study are available within the paper and corresponding references. Any further information or clarification is available from the corresponding author upon reasonable request.

Declaration of Competing Interest

The authors declare no competing interests.

CRediT authorship contribution statement

W. Trehern: Visualization, Methodology, Supervision, Funding acquisition, Formal analysis, Data curation, Writing – original draft, Writing – review & editing. **R. Ortiz-Ayala:** Funding acquisition, Formal analysis, Data curation, Writing – review & editing. **K.C. Atli:** Funding acquisition, Formal analysis, Data curation, Writing – original draft, Writing – review & editing. **R. Arroyave:** Writing – original draft, Writing – review & editing. **I. Karaman:** Visualization, Writing – original draft, Writing – review & editing.

Acknowledgments

The authors would like to acknowledge the support of the Data-Enabled Discovery and Design of Energy Materials (D^3EM) program funded by NSF through Grant No. DGE-1,545,403. RA and IK also acknowledge the support from NSF under Grant No. 2,119,103 (DMREF: AI-Guided Accelerated Discovery of Multi-Principal Element Multi-Functional Alloys).

Supplementary materials

Supplementary material associated with this article can be found, in the online version, at doi:10.1016/j.actamat.2022.117751.

References

[1] K. Otsuka, C.M. Wayman, Shape Memory Materials, Cambridge University Press, 1999.
[2] D.C. Lagoudas, Shape Memory Alloys: Modeling and Engineering Applications, Springer, 2008.
[3] J. Ma, I. Karaman, R.D. Noebe, High temperature shape memory alloys, Int. Mater. Rev. 55 (5) (2010) 257–315.
[4] J. Cui, Y.S. Chu, O.O. Famodu, Y. Furuya, J. Hattrick-Simpers, R.D. James, A. Ludwig, S. Thienhaus, M. Wuttig, Z. Zhang, Combinatorial search of thermoelastic shape-memory alloys with extremely small hysteresis width, Nat. Mater. 5 (4) (2006) 286–290.
[5] Y. Song, X. Chen, V. Dabade, T.W. Shield, R.D. James, Enhanced reversibility and unusual microstructure of a phase-transforming material, Nature 502 (7469) (2013) 85–88.
[6] J. Ma, I. Karaman, Expanding the repertoire of shape memory alloys, Science 327 (5972) (2010) 1468–1469.
[7] M. Gueltig, H. Ossmer, M. Ohtsuka, H. Miki, K. Tsuchiya, T. Takagi, M. Kohl, High frequency thermal energy harvesting using magnetic shape memory films, Adv. Energy Mater. 4 (17) (2014) 1400751.
[8] I. Karaman, B. Basaran, H. Karaca, A. Karsilayan, Y. Chumlyakov, Energy harvesting using martensite variant reorientation mechanism in a NiMnGa magnetic shape memory alloy, Appl. Phys. Lett. 90 (17) (2007) 172505.
[9] B. Gusarov, E. Gusarova, B. Viala, L. Gimeno, S. Boisseau, O. Cugat, E. Vandelle, B. Louison, Thermal energy harvesting by piezoelectric PVDF polymer coupled with shape memory alloy, Sens. Actuators A Phys. 243 (2016) 175–181.
[10] J. Ortin, A. Planes, Thermodynamic analysis of thermal measurements in thermoelastic martensitic transformations, Acta Metall. 36 (8) (1988) 1873–1889.
[11] J. Frenzel, A. Wieczorek, I. Opahle, B. Maaß, R. Drautz, G. Eggeler, On the effect of alloy composition on martensite start temperatures and latent heats in Ni–Ti-based shape memory alloys, Acta Mater. 90 (2015) 213–231.
[12] Z. Zhang, R.D. James, S. Müller, Energy barriers and hysteresis in martensitic phase transformations, Acta Mater. 57 (15) (2009) 4332–4352.
[13] J. Khalil-Allafi, A. Dlouhy, G. Eggeler, Ni_4Ti_3-precipitation during aging of NiTi shape memory alloys and its influence on martensitic phase transformations, Acta Mater. 50 (17) (2002) 4255–4274.

[14] D.A. Miller, D.C. Lagoudas, Influence of cold work and heat treatment on the shape memory effect and plastic strain development of NiTi, Mater. Sci. Eng. A 308 (1–2) (2001) 161–175.
[15] R. Zarnetta, R. Takahashi, M.L. Young, A. Savan, Y. Furuya, S. Thienhaus, B. Maaß, M. Rahim, J. Frenzel, H. Brunken, Identification of quaternary shape memory alloys with near-zero thermal hysteresis and unprecedented functional stability, Adv. Funct. Mater. 20 (12) (2010) 1917–1923.
[16] H. Li, X. Meng, W. Cai, Shape memory behaviors in a $Ti_{50}Ni_{33.5}Cu_{12.5}Pd_4$ alloy with near-zero thermal hysteresis, J. Alloy. Compd. 765 (2018) 166–170.
[17] R.D. James, K.F. Hane, Martensitic transformations and shape-memory materials, Acta Mater. 48 (1) (2000) 197–222.
[18] M. Zarinejad, Y. Liu, Dependence of transformation temperatures of Ni-Ti-based shape-memory alloys on the number and concentration of valence electrons, Adv. Funct. Mater. 18 (18) (2008) 2789–2794.
[19] Y. Ye, C.T. Chan, K.M. Ho, Structural and electronic properties of the martensitic alloys TiNi, TiPd, and TiPt, Phys. Rev. B 56 (7) (1997) 3678.
[20] J.M. Ball, C. Chu, R.D. James, Hysteresis during stress-induced variant rearrangement, J. Phys. IV 5 (C8) (1995) 245–251 C8-245-C8-251.
[21] K. Atli, B. Franco, I. Karaman, D. Gaydosh, R. Noebe, Influence of crystallographic compatibility on residual strain of TiNi based shape memory alloys during thermo-mechanical cycling, Mater. Sci. Eng. A 574 (2013) 9–16.
[22] P. Potapov, A. Shelyakov, A. Gulyaev, E. Svistunov, N. Matveeva, D. Hodgson, Effect of Hf on the structure of Ni-Ti martensitic alloys, Mater. Lett. 32 (4) (1997) 247–250.
[23] A. Evirgen, I. Karaman, R. Santamarta, J. Pons, C. Hayrettin, R. Noebe, Relationship between crystallographic compatibility and thermal hysteresis in Ni-rich NiTiHf and NiTiZr high temperature shape memory alloys, Acta Mater. 121 (2016) 374–383.
[24] N. Ozdemir, I. Karaman, N. Mara, Y.I. Chumlyakov, H. Karaca, Size effects in the superelastic response of $Ni_{54}Fe_{19}Ga_{27}$ shape memory alloy pillars with a two stage martensitic transformation, Acta Mater. 60 (16) (2012) 5670–5685.
[25] H. Zong, Z. Ni, X. Ding, T. Lookman, J. Sun, Origin of low thermal hysteresis in shape memory alloy ultrathin films, Acta Mater. 103 (2016) 407–415.
[26] H. Sehitoglu, R. Hamilton, H. Maier, Y. Chumlyakov, Hysteresis in NiTi alloys, J. Phys. IV (Proceedings) 115 (2004) 3–10 EDP sciences.
[27] R.F. Hamilton, H. Sehitoglu, Y. Chumlyakov, H.J. Maier, Stress dependence of the hysteresis in single crystal NiTi alloys, Acta Mater. 52 (11) (2004) 3383–3402.
[28] K. Rajan, Materials informatics: the materials "gene" and big data, Annu. Rev. Mater. Res. 45 (2015) 153–169.
[29] Y. Liu, T. Zhao, W. Ju, S. Shi, Materials discovery and design using machine learning, J. Mater. 3 (3) (2017) 159–177.
[30] Y. Liu, J. Wu, G. Yang, T. Zhao, S. Shi, Predicting the onset temperature (Tg) of GexSe1− x glass transition: a feature selection based two-stage support vector regression method, Sci. Bull. 64 (16) (2019) 1195–1203.
[31] D. Xue, R. Yuan, Y. Zhou, D. Xue, T. Lookman, G. Zhang, X. Ding, J. Sun, Design of high temperature Ti-Pd-Cr shape memory alloys with small thermal hysteresis, Sci. Rep. 6 (2016) 28244.
[32] D. Xue, Y. Tian, R. Yuan, T. Lookman, Bayesian global optimization applied to the design of shape-memory alloys, in: Uncertainty Quantification in Multiscale Materials Modeling, Elsevier, 2020, pp. 519–537.
[33] D. Xue, D. Xue, R. Yuan, Y. Zhou, P.V. Balachandran, X. Ding, J. Sun, T. Lookman, An informatics approach to transformation temperatures of NiTi-based shape memory alloys, Acta Mater. 125 (2017) 532–541.
[34] D. Xue, P.V. Balachandran, J. Hogden, J. Theiler, D. Xue, T. Lookman, Accelerated search for materials with targeted properties by adaptive design, Nat. Commun. 7 (1) (2016) 1–9.
[35] S. Liu, B.B. Kappes, B. Amin-ahmadi, O. Benafan, X. Zhang, A.P. Stebner, Physics-informed machine learning for composition – process – property design: shape memory alloy demonstration, Appl. Mater. Today 22 (2021) 100898.
[36] X.. Zhao, H.Y. Huang, C. Wen, Y.J. Su, P. Qian, Accelerating the development of multi-component Cu-Al-based shape memory alloys with high elastocaloric property by machine learning, Comput. Mater. Sci. 176 (2020) 109521.
[37] A.J. Kadic, K. Vucic, S. Dosenovic, D. Sapunar, L. Puljak, Extracting data from figures with software was faster, with higher interrater reliability than manual extraction, J. Clin. Epidemiol. 74 (2016) 119–123.
[38] V. Tshitoyan, J. Dagdelen, L. Weston, A. Dunn, Z. Rong, O. Kononova, K.A. Persson, G. Ceder, A. Jain, Unsupervised word embeddings capture latent knowledge from materials science literature, Nature 571 (7763) (2019) 95–98.
[39] B.P. MacLeod, F.G. Parlane, T.D. Morrissey, F. Häse, L.M. Roch, K.E. Dettelbach, R. Moreira, L.P. Yunker, M.B. Rooney, J.R. Deeth, Self-driving laboratory for accelerated discovery of thin-film materials, Sci. Adv. 6 (20) (2020) eaaz8867.
[40] L.M. Ghiringhelli, J. Vybiral, S.V. Levchenko, C. Draxl, M. Scheffler, Big data of materials science: critical role of the descriptor, Phys. Rev. Lett. 114 (10) (2015) 105503.
[41] S.P. Ong, W.D. Richards, A. Jain, G. Hautier, M. Kocher, S. Cholia, D. Gunter, V.L. Chevrier, K.A. Persson, G. Ceder, Python materials genomics (pymatgen): a robust, open-source python library for materials analysis, Comput. Mater. Sci. 68 (2013) 314–319.
[42] M.A. Hall, Correlation-based feature selection for machine learning, *PhD Thesis*, New Zealand Department of Computer Science, Waikato University (1999).
[43] S.T. Roweis, L.K. Saul, Nonlinear dimensionality reduction by locally linear embedding, Science 290 (5500) (2000) 2323–2326.
[44] S. Wold, K. Esbensen, P. Geladi, Principal component analysis, Chemom. Intell. Lab. Syst. 2 (1–3) (1987) 37–52.
[45] G. Lemaître, F. Nogueira, C.K. Aridas, Imbalanced-learn: a python toolbox to tackle the curse of imbalanced datasets in machine learning, J. Mach. Learn. Res. 18 (1) (2017) 559–563.
[46] J.R. Quinlan, Induction of decision trees, Mach. Learn. 1 (1) (1986) 81–106.
[47] R. Ouyang, S. Curtarolo, E. Ahmetcik, M. Scheffler, L.M. Ghiringhelli, SISSO: a compressed-sensing method for identifying the best low-dimensional descriptor in an immensity of offered candidates, Phys. Rev. Mater. 2 (8) (2018) 083802.
[48] T. Ueno, T.D. Rhone, Z. Hou, T. Mizoguchi, K. Tsuda, COMBO: an efficient Bayesian optimization library for materials science, Mater. Discov. 4 (2016) 18–21.
[49] J. Snoek, H. Larochelle, R.P. Adams, Practical bayesian optimization of machine learning algorithms, Adv. Neural Inf. Process. Syst. 25 (2012) 2951–2959.
[50] K. Deb, A. Pratap, S. Agarwal, T. Meyarivan, A fast and elitist multiobjective genetic algorithm: NSGA-II, IEEE Trans. Evol. Comput. 6 (2) (2002) 182–197.
[51] K. Deb, Multi-objective Optimization Using Evolutionary Algorithms, John Wiley & Sons, 2001.
[52] M. Laumanns, J. Ocenasek, Bayesian optimization algorithms for multi-objective optimization, in: Proceedings of the International Conference on Parallel Problem Solving from Nature, Springer, 2002, pp. 298–307.
[53] F.A. Viana, G. Venter, V. Balabanov, An algorithm for fast optimal Latin hypercube design of experiments, Int. J. Numer. Methods Eng. 82 (2) (2010) 135–156.
[54] V. Pushin, N. Kuranova, E. Marchenkova, A. Pushin, Design and development of Ti–Ni, Ni–Mn–Ga and Cu–Al–Ni-based alloys with high and low temperature shape memory effects, Materials 12 (16) (2019) 2616 (Basel).
[55] X. Shu, S. Lu, G. Li, J. Liu, P. Peng, Nb solution influencing on phase transformation temperature of Ni47Ti44Nb9 alloy, J. Alloy. Compd. 609 (2014) 156–161.
[56] Y. Chen, H. Jiang, S. Liu, L. Rong, X. Zhao, The effect of Mo additions to high damping Ti–Ni–Nb shape memory alloys, Mater. Sci. Eng. A 512 (1–2) (2009) 26–31.
[57] J. Wang, T. Omori, Y. Sutou, R. Kainuma, K. Ishida, Two-way shape memory effect induced by cold-rolling in Ti–Ni and Ti–Ni–Fe alloys, Scr. Mater. 52 (4) (2005) 311–316.
[58] J. Wang, F. Liu, J. Cao, The microstructure and thermomechanical behavior of $Ti_{50}Ni_{47}Fe_{2.5}Nd_{0.5}$ shape memory alloys, Mater. Sci. Eng. A 527 (23) (2010) 6200–6204.
[59] B. Lin, K. Gall, H.J. Maier, R. Waldron, Structure and thermomechanical behavior of NiTiPt shape memory alloy wires, Acta Biomater. 5 (1) (2009) 257–267.
[60] L. Meisner, V. Sivokha, The effect of applied stress on the shape memory behavior of TiNi-based alloys with different consequences of martensitic transformations, Phys. B Condens. Matter 344 (1–4) (2004) 93–98.
[61] K. Atli, I. Karaman, R. Noebe, Work output of the two-way shape memory effect in $Ti_{50.5}Ni_{24.5}Pd_{25}$ high-temperature shape memory alloy, Scr. Mater. 65 (10) (2011) 903–906.
[62] W. Cai, S. Tanaka, K. Otsuka, Thermal cyclic characteristics under load in a $Ti_{50.6}Pd_{30}Ni_{19.4}$ alloy, Mater. Sci. Forum 31 (2000) 279–282.
[63] K. Atli, I. Karaman, R. Noebe, D. Gaydosh, The effect of training on two-way shape memory effect of binary NiTi and NiTi based ternary high temperature shape memory alloys, Mater. Sci. Eng. A 560 (2013) 653–666.
[64] Y. Hattori, T. Taguchi, H.Y. Kim, S. Miyazaki, Effect of stoichiometry on shape memory properties and functional stability of Ti–Ni–Pd alloys, Materials 12 (5) (2019) 798 (Basel).
[65] D.H. Dai Hsu, T.T. Sasaki, G.B. Thompson, M.V. Manuel, The effect of aluminum additions on the microstructure and thermomechanical behavior of NiTiZr shape-memory alloys, Metall. Mater. Trans. A 43 (8) (2012) 2921–2931.
[66] A. Pérez-Sierra, J. Pons, R. Santamarta, I. Karaman, R. Noebe, Stability of a Ni-rich Ni-Ti-Zr high temperature shape memory alloy upon low temperature aging and thermal cycling, Scr. Mater. 124 (2016) 47–50.
[67] A. Evirgen, I. Karaman, J. Pons, R. Santamarta, R. Noebe, Role of nano-precipitation on the microstructure and shape memory characteristics of a new $Ni_{50.3}Ti_{34.7}Zr_{15}$ shape memory alloy, Mater. Sci. Eng. A 655 (2016) 193–203.
[68] P. Olier, J. Brachet, J. Bechade, C. Foucher, G. Guenin, Investigation of transformation temperatures, microstructure and shape memory properties of NiTi, NiTiZr and NiTiHf alloys, J. Phys. IV 5 (C8) (1995) 741–746 C8-741-C8-746.
[69] A. Sandu, K. Tsuchiya, S. Yamamoto, Y. Todaka, M. Umemoto, Influence of isothermal ageing on mechanical behaviour in Ni-rich Ti–Zr–Ni shape memory alloy, Scr. Mater. 55 (12) (2006) 1079–1082.
[70] M. Azeem, D. Dye, *In situ* evaluation of the transformation behaviour of Ni-Ti-based high temperature shape memory alloys, Intermetallics 46 (2014) 222–230.
[71] G. Firstov, J. Van Humbeeck, Y.N. Koval, Comparison of high temperature shape memory behaviour for ZrCu-based, Ti–Ni–Zr and Ti–Ni–Hf alloys, Scr. Mater. 50 (2) (2004) 243–248.
[72] S. Hsieh, S. Wu, A study on ternary Ti-rich TiNiZr shape memory alloys, Mater. Charact. 41 (4) (1998) 151–162.
[73] A. Nespoli, E. Villa, S. Besseghini, Characterization of the martensitic transformation in Ni50− xTi50Cux alloys through pure thermal measurements, J. Alloy. Compd. 509 (3) (2011) 644–647.
[74] Y.H. Li, L.J. Rong, Z.T. Wang, G.X. Qi, C.Z. Wang, Temperature memory effect of $Ti_{50}Ni_{30}Cu_{20}$ (at.%) alloy, J. Alloy. Compd. 400 (1–2) (2005) 112–115.
[75] S. Tan, S. Miyazaki, T. Ueki, H. Horikawa, Ti-content and annealing temperature dependence of transformation behavior of TiXNi (92-XCu8 shape memory alloys, Mater. Sci. Eng. A 230 (1–2) (1997) 132–138.

[76] Z. Zhang, J. Frenzel, K. Neuking, G. Eggeler, Vacuum induction melting of ternary NiTiX (X= Cu, Fe, Hf, Zr) shape memory alloys using graphite crucibles, Mater. Trans. 47 (3) (2006) 661–669.
[77] C.M. Denowh, D.A. Miller, Thermomechanical training and characterization of Ni–Ti–Hf and Ni–Ti–Hf–Cu high temperature shape memory alloys, Smart Mater. Struct. 21 (6) (2012) 065020.
[78] D.H. Dai Hsu, B.C. Hornbuckle, B. Valderrama, F. Barrie, H.B. Henderson, G.B. Thompson, M.V. Manuel, The effect of aluminum additions on the thermal, microstructural, and mechanical behavior of NiTiHf shape memory alloys, J. Alloy. Compd. 638 (2015) 67–76.
[79] D. Canadinc, W. Trehern, H. Ozcan, C. Hayrettin, O. Karakoc, I. Karaman, F. Sun, Z. Chaudhry, On the deformation response and cyclic stability of $Ni_{50}Ti_{35}Hf_{15}$ high temperature shape memory alloy wires, Scr. Mater. 135 (2017) 92–96.
[80] A. Evirgen, I. Karaman, R. Santamarta, J. Pons, R. Noebe, Microstructural characterization and shape memory characteristics of the $Ni_{50.3}Ti_{34.7}Hf_{15}$ shape memory alloy, Acta Mater. 83 (2015) 48–60.
[81] X. Yi, W. Gao, X. Meng, Z. Gao, W. Cai, L. Zhao, Martensitic transformation behaviors and mechanical properties of $(Ti_{36}Ni_{49}Hf_{15})_{100-x}Yx$ high temperature shape memory alloys, J. Alloy. Compd. 705 (2017) 98–104.
[82] H. Karaca, S. Saghaian, G. Ded, H. Tobe, B. Basaran, H. Maier, R. Noebe, Y. Chumlyakov, Effects of nanoprecipitation on the shape memory and material properties of an Ni-rich NiTiHf high temperature shape memory alloy, Acta Mater. 61 (19) (2013) 7422–7431.
[83] B. Kockar, I. Karaman, J. Kim, Y. Chumlyakov, A method to enhance cyclic reversibility of NiTiHf high temperature shape memory alloys, Scr. Mater. 54 (12) (2006) 2203–2208.
[84] D. Canadinc, W. Trehern, J. Ma, I. Karaman, F. Sun, Z. Chaudhry, Ultra-high temperature multi-component shape memory alloys, Scr. Mater. 158 (2019) 83–87.
[85] R. Delville, S. Kasinathan, Z. Zhang, J.V. Humbeeck, R.D. James, D. Schryvers, Transmission electron microscopy study of phase compatibility in low hysteresis shape memory alloys, Philos. Mag. 90 (1–4) (2010) 177–195.
[86] Y. Liu, J. Laeng, T. Chin, T.H. Nam, Effect of incomplete thermal cycling on the transformation behaviour of NiTi, Mater. Sci. Eng. A 435 (2006) 251–257.
[87] Z. Wang, X. Zu, S. Zhu, L. Wang, Temperature memory effect induced by incomplete transformation in TiNi shape memory alloy, Mater. Lett. 59 (4) (2005) 491–494.
[88] L. Sun, W. Huang, J. Cheah, The temperature memory effect and the influence of thermo-mechanical cycling in shape memory alloys, Smart Mater. Struct. 19 (5) (2010) 055005.
[89] H. Abdi, L.J. Williams, Principal component analysis, Wiley Interdiscip. Rev. Comput. Stat. 2 (4) (2010) 433–459.
[90] N.V. Chawla, K.W. Bowyer, L.O. Hall, W.P. Kegelmeyer, SMOTE: synthetic minority over-sampling technique, J. Artif. Intell. Res. 16 (2002) 321–357.
[91] T. Chen, C. Guestrin, Xgboost: a scalable tree boosting system, in: Proceedings of the 22nd ACM SIGKDD International Conference on Knowledge Discovery and Data Mining, 2016, pp. 785–794.
[92] J. Bergstra, D. Yamins, D.D. Cox, Hyperopt: a python library for optimizing the hyperparameters of machine learning algorithms, in: Proceedings of the 12th Python in Science Conference, 2013, p. 20. Citeseer.
[93] V. Nair, G.E. Hinton, Rectified linear units improve restricted boltzmann machines, in: Proceedings of the ICML, 2010.
[94] N. Srivastava, G. Hinton, A. Krizhevsky, I. Sutskever, R. Salakhutdinov, Dropout: a simple way to prevent neural networks from overfitting, J. Mach. Learn. Res. 15 (1) (2014) 1929–1958.
[95] N. Islam, W. Huang, H.L. Zhuang, Machine learning for phase selection in multi-principal element alloys, Comput. Mater. Sci. 150 (2018) 230–235.
[96] F. Chollet, Keras. https://github.com/fchollet/keras.
[97] M. Abadi, et al., Tensorflow: large-scale machine learning on heterogeneous distributed systems, Preprint (2016) https://arxiv.org/abs/1603.04467.
[98] L. Casalena, G.S. Bigelow, Y. Gao, O. Benafan, R.D. Noebe, Y. Wang, M.J. Mills, Mechanical behavior and microstructural analysis of NiTi-40Au shape memory alloys exhibiting work output above 400 C, Intermetallics 86 (2017) 33–44.
[99] T.H. Nam, T. Saburi, Y. Nakata, K.I. Shimizu, Shape memory characteristics and lattice deformation in Ti–Ni–Cu alloys, Mater. Trans. 31 (12) (1990) 1050–1056 JIM.
[100] W.J. Zhu, L.I. Duarte, C. Leinenbach, Experimental study and thermodynamic assessment of the Cu–Ni–Ti system, Calphad 47 (2014) 9–22.
[101] C. Chluba, W. Ge, R.L. de Miranda, J. Strobel, L. Kienle, E. Quandt, M. Wuttig, Ultralow-fatigue shape memory alloy films, Science 348 (6238) (2015) 1004–1007.
[102] H. Gu, L. Bumke, C. Chluba, E. Quandt, R.D. James, Phase engineering and supercompatibility of shape memory alloys, Mater. Today 21 (3) (2018) 265–277.
[103] D.G. Pettifor, A chemical scale for crystal-structure maps, Solid State Commun. 51 (1) (1984) 31–34.
[104] D. Pettifor, The structures of binary compounds. I. Phenomenological structure maps, J. Phys. C Solid State Phys. 19 (3) (1986) 285.